Solar Energy 178 (2019) 162–172

Contents lists available at ScienceDirect

Solar Energy

journal homepage: www.elsevier.com/locate/solener

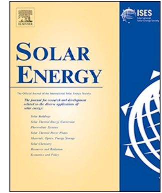

Elucidating the role of interfacial MoS_2 layer in Cu_2ZnSnS_4 thin film solar cells by numerical analysis

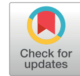

M.T. Ferdaous[a,1], S.A. Shahahmadi[b,*,1], P. Chelvanathan[c,*], Md. Akhtaruzzaman[c], F.H. Alharbi[d], K. Sopian[c], S.K. Tiong[b], N. Amin[a,b]

[a] Department of Electrical, Electronics and System Engineering, The National University of Malaysia, 43600 Bangi, Selangor, Malaysia
[b] Institute of Sustainable Energy (ISE), Universiti Tenaga Nasional (@The National Energy University), Jalan IKRAM-UNITEN, 43000 Kajang, Selangor, Malaysia
[c] Solar Energy Research Institute (SERI), The National University of Malaysia, 43600 Bangi, Selangor, Malaysia
[d] Qatar Environment and Energy Research Institute (QEERI), Hamad Bin Khalifa University (HBKU), Qatar Foundation, P.O. Box 5825, Doha, Qatar

ARTICLE INFO

Keywords:
Cu_2ZnSnS_4 solar cells
MoS_2 interfacial layer
Charge carrier transports
Numerical analysis

ABSTRACT

In this study, the effects of transition metal dichalcogenide, MoS_2 interfacial layer formation between the Cu_2ZnSnS_4 (CZTS) absorber layer and Mo back contact in a conventional CZTS thin film solar cell (TFSC) structure have been studied by numerical simulation using wxAMPS-1D software. The goal of this study is to elucidate the effects of both n and p-type MoS_2 on the overall CZTS solar cell's performance from the viewpoint of metal-semiconductor junction and heterojunction band alignment. Interestingly, CZTS device, regardless of p or n-type MoS_2 largely outperforms device without any MoS_2 due to lower back contact barrier value. Significant transition in efficiency is noticed when acceptor (increases efficiency) or donor (decreases efficiency) concentration has a transition from 10^{16} cm^{-3} to higher concentration of 10^{18} cm^{-3} or more. Also, effect of variable electron affinity and band gap of MoS_2 has been discussed from band alignment perspective. Generally, MoS_2 layer with lower electron affinity and band gap is preferred to induce desirable band alignment and subsequently result in higher efficiency. All-in all, the formation of p-type MoS_2 in CZTS solar cells can be tuned to improve the cell performance mainly by doping with higher acceptor doping concentration and limiting layer thickness. However, the detrimental effect of n-MoS_2 can be prevented by maintaining thinner layer in the vicinity of ~30 nm with low to moderate donor doping (< 10^{16} cm^{-3}).

1. Introduction

Cu_2ZnSnS_4 (CZTS) thin film solar cell (TFSC) is an emerging and potential candidate for carbon free electricity generation of the future. The p-type kesterite absorber layer is made up of copper (Cu), zinc (Zn), tin (Sn) and sulphur (S) elements, which are earth-abundant and non-toxic (Katagiri, 2005). Hence CZTS TFSC is a promising candidate as a low-cost replacement of Cu(In,Ga)Se_2 (CIGS) TFSC that incorporates expensive rare-earth elements such as indium (In) and gallium (Ga). Cu-chalcopyrite, especially the CIGS TFSC has achieved the highest power conversion efficiency (PCE) of nearly 22.9% compared to 11.5% in case of CZTS TFSC (Green et al., 2018; Yan et al., 2017). Some main challenges such as undesirable band alignment at the CZTS/buffer hetero-interface, unwanted secondary and ternary phases in the CZTS absorber layer, and the presence of an interfacial type MoS_2 layer at Mo/CZTS have been long attributed as performance limiting factors of this quaternary TFSCs (Chelvanathan et al., 2018; Sun et al., 2016; Scragg et al., 2012; Wätjen et al., 2013). One of the key research findings in the CIGS TFSCs is the ability of CIGS to make ohmic contact with the Mo back contact (Abou-Ras et al., 2005). The formation of the p-type interfacial $MoSe_2$ film with thickness in the range of a few tens of nm is found to facilitate the development of ohmic contact, which is important to reduce series resistance, R_s. Similar beneficial aspect of $MoSe_2$ have been verified by numerical modelling of Mo back contact in Se-containing CZTSe devices (Cozza et al., 2016). On the other hand, unintentional formation of interfacial MoS_2 layer is commonly observed in practical CZTS devices due to the spontaneous reaction between S and Mo back contact.

MoS_2 thin films have been reported to exhibit both p or n-type conductivity. However, MoS_2 has a natural propensity to possess n-type semiconducting characteristics due to the presence native defects of S vacancies which acts as a deep donor (Brahim et al., 2016; Yang et al.,

* Corresponding authors.
E-mail addresses: seyedahmad@uniten.edu.my (S.A. Shahahmadi), cpuvaneswaran@ukm.edu.my (P. Chelvanathan).
[1] These authors have contributed equally in the writing of this paper.

https://doi.org/10.1016/j.solener.2018.11.055
Received 16 September 2018; Received in revised form 18 November 2018; Accepted 21 November 2018
Available online 19 December 2018
0038-092X/ © 2018 Elsevier Ltd. All rights reserved.

2015; Wei et al., 2018). By incorporation of suitable dopants such as phosphorous (Nipane et al., 2016), oxygen (Neal et al., 2017), and niobium (Laskar et al., 2014; Suh et al., 2014) as substitutional acceptors, p-type semiconducting characteristics in the MoS_2 layer have been reported. However, the electrical conductivity nature of MoS_2 interfacial layer which is sandwiched between Mo and CZTS in CZTS TFSCs has not been conclusively determined by any experimental method so far. Although, the conductivity of MoS_2 grown by sulfurization of Mo thin film has been conclusively determined as the n-type (Dhakal et al., 2015). In addition to this, inferring from the outcome of our preceding numerical study, formation of n-MoS_2 is most likely to be responsible for the commonly observed high R_s and low fill factor (FF) (Puvaneswaran et al., 2012). Several attempts to inhibit or passivate this interfacial layer through an insertion of thin intermediate layer such as SnS, ZnO, TiN, Al_2O_3, or preferential heat treatment of Mo back contact have been stated (Chelvanathan et al., 2018; Cui et al., 2014; Chen et al., 2016; Yang et al., 2015; Li et al., 2014; Liu et al., 2017). However, no practical experimental effort has been studied yet to tailor or induce p-type conductivity in the interfacial MoS_2 layer in order to engineer favorable ohmic charge carrier transport mimicking the adventitious p-$MoSe_2$ in CIGS devices.

Therefore, as an extension of our previous study (Puvaneswaran et al., 2012), this work primarily focuses on the comparative investigation on the effects of p-type and n-type interfacial layers of MoS_2 in the CZTS TFSCs. Since electronic band structure properties mainly electron affinity (χ) and band gap (E_g) of MoS_2 are profoundly dependent on the layer thickness (Komsa and Krasheninnikov, 2015), both monolayers and bulk structured MoS_2 are considered in this numerical analysis. Detailed Mo/MoS_2/CZTS band alignment configurations are constructed for all simulated cases and pertinent interface related electronic properties are calculated. We numerically show that n-type MoS_2 interfacial layer with low donor density acts as a considerably benign component, whereas, p-type MoS_2 interfacial layer generally induces beneficial back contact carrier transport characteristics and subsequently improve the CZTS TFSCs performance. The key outcomes outlined in study is expected to initiate experimental efforts to incorporate p-type MoS_2 as back contact buffer layer in CZTS TFSC and other emerging S containing absorber layer with similar electronic band structure properties.

2. Methodology

In this numerical study, wxAMPS-1D software is used to simulate the effects of MoS_2 layer formation in the Mo/MoS_2/CZTS/CdS/i-ZnO/Al substrate type configured TFSC. Information about wxAMPS-1D is given elsewhere (Hossain et al., 2018) while the structure of CZTS TFSC is similar to the conventional CIGS's structure as used in the literature (Amin et al., 2010; Chelvanathan et al., 2017; Hossain et al., 2013). Formation of interfacial MoS_2 layer is expected to predominantly influence the electronic band alignment at the metal/semiconductor junction of Mo/MoS_2 and semiconductor/semiconductor heterojunction of MoS_2/CZTS. The band structure of MoS_2 varies with multilayer thickness, transitioning from ~1.98 eV direct E_g in a single layer to ~1.27 eV indirect E_g in multilayer and bulk presentation (Yim et al., 2014; Dileep et al., 2016). Decoupling of MoS_2 layers upon increasing the number of layers causes significant changes in the shapes of valence and conduction bands. These remarkable changes of the band structure are directly related to the orbital composition of involved electronic states (Yazyev and Kis, 2015). In general, transport and optoelectrical properties of the host material are profoundly influenced by lattice point defects like vacancies and interstitials, which would act as very efficient traps for electrons, holes, and excitons. Radiative recombination of excitons that are bounded to defects leads to light emission at energies lower than the band-to-band optical transition energy. Such interactions become stronger in reduced dimensionalities due to tighter localization of the electron wave function. These defects have been explained by various techniques like electron spin resonance (Daniele et al., 2016) or observation on phase diagram (Reale et al., 2016). Depending on the number of MoS_2 layers, the associated defect density lies between 6×10^{11} and 3×10^{12} cm^2 (Tongay et al., 2013), which shows the high purity in this ultrathin (< 10 nm) two-dimensional material. However, the evolution of a new extrinsically induced defect state in the E_g brings to light essentially unexplored opportunities for modifying the optoelectronic properties through control of defect density, type, and distribution (Chow et al., 2015).

The experimentally reported χ in bulk MoS_2 crystals is about 4.0 eV (Schlaf et al., 1999), and it is known that an enlarged E_g with decreased χ is expected in MoS_2 with decreasing number of layers (Qiu et al., 2012; Kang et al., 2013). However, the calculated χ of monolayer MoS_2 is 4.27 eV (Gong et al., 2013), which reflects the challenges in calculating and measuring the absolute positions of energy bands using first principles computations and experiments, respectively. Overall, reported values for the χ in MoS_2 range from 3.74 to 4.45 eV (Howell et al., 2015), depending on MoS_2 thickness and measurement techniques. Similarly, a large range of values for dielectric constant is found, which is dependent on the outcomes of different experiments and methods of modeling (from 2.5 to 17 (Dashora et al., 2013; Santos and Kaxiras, 2013)). Dielectric constant increases with the thickness of the thin films and these values for 8 or higher numbers of layers are comparable with the bulk material values, suggesting that a film of 8 layers (thickness of ~4.9 nm) of MoS_2 is sufficient for economical fabrication of solar cells (Dashora et al., 2013). Literature survey reveals that mobility values, which are often used to gauge the quality of the material and devices, can vary from 1 to 34,000 $cm^2\ V^{-1}\cdot s^{-1}$ (Cui et al., 2015; Kappera et al., 2014). The large deviation in mobility values arises from intrinsic challenges of forming good ohmic contacts and large discrepancies in device fabrication and measurement procedures. Another important aspect of MoS_2 is the ability to be doped with a shallow acceptor or donor level, respectively. In experiment, controllable and stable doping process is the major device-related challenge for MoS_2 since it influences other parameters (Wang et al., 2017).

With all that being said, it is clear that optoelectrical properties of MoS_2 is highly dependent on the layer thickness, deposition methods, and measurement techniques. Thus, defining precise material properties based on the variation of thickness is very complex and subjective. We assumed that all material properties of MoS_2 layer in the range of 10–300 nm thickness are similar to the bulk mode of MoS_2 while distinct material properties are adopted for monolayer MoS_2. Absorption coefficients of MoS_2 were generated by the software's model and cutoff frequency was estimated based on the optical E_g value. Defect states degrade the optoelectronic quality and any changes in their values would affect optoelectronic properties. Since the electronic band alignment can be profoundly changed by simply altering electronic properties in wxAMPS-1D, adding appropriate defect's parameters rather than a constant value will further compound the changes in the overall energy band line-up, which is not the scope this work and will be investigated in our future work. Hence, in order to solely accentuate the effects of carrier concentration, E_g, and χ of MoS_2 on the PCE, open circuit voltage (V_{oc}), short circuit current (J_{sc}), and FF of the simulated device, defect-free layers are assumed in this study. Furthermore, CdS/CZTS interface recombination, CZTS bandgap narrowing, and short diffusion length phenomena are not incorporated in this simulation with the aim of masking the influence of the aforementioned material and device characteristics from the numerical outcome. For detailed explanation on effects of the aforesaid phenomena on the CZTS device, readers are encouraged to peruse the work from Frisk et al. (2016). The first part of this simulation study elucidates the combinatorial effects of variable carrier concentration from 10^{13} to 10^{19} cm^{-3} and thickness from monolayer to bulk for both n and p type MoS_2. On the other hand, hypothetical study based on variation of E_g and χ from 1.2 to 1.7 eV and 3.9 to 4.6 eV for both n and p-type MoS_2 due to the reported difficulties to measure E_g and χ (Howell et al., 2015; Shahahmadi et al.,

Table 1
Material electronic properties used in simulation.

Interface Parameters	Front			Back			
Barrier height Φ_b (eV)	$\Phi_{bn} = 0$			0.23	0.5	0.6-(−0.1)	0.5
Electron surface recombination Velocity, S_e (cm s^{-1})	10^7			10^7		10^7	10^7
Hole surface recombinationVelocity, S_h (cm s^{-1})	10^7			10^7		10^7	10^7
Reflectivity	0.05			0.80		0.80	0.80
Layer parameters	ZnO	CdS	CZTS	MoS_2			
				1	2	3	4
Layer thickness (nm)	200	50	2500	0.615	10–300	50	50
Dielectric constant, ε_r	9	10	13.5	2.45	12.61	12.61	12.61
Electron mobility, μ_n (cm^2/V s)	100	100	100	100		100	100
Hole mobility, μ_p (cm^2/V s)	25	25	25	25		25	25
Acceptor concentration, N_A (cm^{-3})	0	0	10^{18}	10^{13}–10^{19}		10^{16}&10^{18}	10^{16}&10^{18}
Donor concentration, N_D (cm^{-3})	10^{18}	10^{18}	0				
Band gap, E_g (eV)	3.30	2.4	1.5	1.98	1.27	1.27	1.2–1.7
Effective density of states in Conduction band, N_C (cm^{-3})	2.2×10^{18}	2.2×10^{18}	2.2×10^{18}	2.2×10^{18}		2.2×10^{18}	2.2×10^{18}
Effective density of states in Valence band, N_V (cm^{-3})	1.8×10^{19}	1.8×10^{19}	1.8×10^{19}	1.8×10^{19}		1.8×10^{19}	1.8×10^{19}
Electron affinity, χ (eV)	4.4	4.2	4.21	4.27	4	3.9–4.6	4

2015) are presented in the remaining last part. The optimum thickness and carrier concentration are obtained from the first part while the explorative outcomes of the hypothesis are derived from last part, respectively. Material electronic parameters used in this study are given as listed in Table 1.

Interface electronic properties such as back contact barrier height with respect to E_c (Φ_{Bn}), back contact barrier height with respect to E_v (Φ_{Bp}), equilibrium contact potential (qV_o), conduction band offset, CBO (ΔE_c), valence band offset, VBO (ΔE_v), and back diode built-in voltage ($qV_{bi_{back}}$) were calculated using the Eqs. (1)–(7). It is noteworthy that the CBO and VBO were calculated according to Anderson's rule (Anderson, 1960).

$$\Phi_{Bn} = \Phi_{Mo} - \chi_s \tag{1}$$

$$\Phi_{Bp} = E_g - \Phi_{Bn} \tag{2}$$

$$qV_o = \Phi_{Mo} - \Phi_s;\ \ \text{for n} - \text{type semiconductor/metal junction} \tag{3}$$

$$qV_o = \Phi_s - \Phi_{Mo};\ \ \text{for p} - \text{type semiconductor/metal junction} \tag{4}$$

$$\Delta E_c = \chi_{CZTS} - \chi_{MoS_2};\ \ \text{for } MoS_2/CZTS \text{ heterojunction} \tag{5}$$

$$\Delta E_v = \left(\chi_{MoS_2} + E_{gMoS_2}\right) - (\chi_{CZTS} + E_{gCZTS});\ \ \text{for } MoS_2/CZTS \text{ heterojunction} \tag{6}$$

$$qV_{bi_{back}} = \Phi_{MoS_2} - \Phi_{CZTS};\ \ \text{for } MoS_2/CZTS \text{ heterojunction} \tag{7}$$

whereby, the Φ_{Mo} is the Mo metal work function while Φ_s is the work function of the semiconductor. The Φ_S of n and p-type semiconductors was calculated according to Eqs. (8) and (9), respectively.

$$\Phi_S = \chi_s + \left(kT\ln\frac{Nc}{N_D}\right);\ \ \text{for n} - \text{type semiconductor} \tag{8}$$

$$\Phi_S = \chi_s + E_g - \left(kT\ln\frac{N_V}{N_A}\right);\ \ \text{for p} - \text{type semiconductor} \tag{9}$$

whereby, q, k, T, N_D, N_A, N_C, and N_V are electron charge, Boltzmann constant, temperature, donor concentration, acceptor concentration, effective density of states in the conduction band and effective density of states in the valence band, respectively. The metal-semiconductor junction can either be ohmic or rectifying depending on the relative magnitude of work function (Φ) of metal and semiconductor (Sze and Ng, 2006). For a Schottky Mo/p-type semiconductor structure, qV_o is the potential barrier retarding hole transport from the semiconductor valence band to metal, meanwhile for a Schottky Mo/n-type semiconductor structure, qV_o is the potential barrier retarding electron transport from the semiconductor conduction band to metal. Values for qV_o are always positive for Schottky type contact and negative for ohmic type contact. Negative (positive) $qV_{bi_{back}}$ indicates the opposite (same) polarity of MoS_2/CZTS heterojunction with respect to the front primary CdS/CZTS heterojunction diode ($qV_{bi_{front}} = \Phi_{CZTS}$-$\Phi_{CdS}$). During solar cell operation under illumination, the conventional charge carrier transport mechanism is as described. Photo-generated electrons in the quasi-neutral region (QNR) of p-CZTS absorber layer initially diffuse towards the CdS/CZTS heterojunction and then drift across the depletion region due to the built-in electric field and finally are collected in the front electrodes. The collected electrons are then supplied to an external circuit whereby power dissipation occurs and finally return to the solar cell via the Mo back contact. Photo-generated holes in the QNR of p-CZTS absorber layer diffuse towards the Mo back contact and recombine with the incoming electrons from the external circuit. Hence, the inclusion of MoS_2 layer in between Mo and CZTS is expected to alter the charge carrier transport dynamics in the back contact region of CZTS TFSC. Although, both Φ_{Bn} and Φ_{Bp} can be calculated (essentially to accentuate the $\Phi_{Bn} + \Phi_{Bp} = E_g$ of MoS_2 relationship) for a particular type of Mo/MoS_2 structure, only one of these parameters is crucially affecting the nature of electron transport across the metal-semiconductor junction. For a Mo/p-MoS_2 metal-semiconductor junction, since the majority carriers in p-MoS_2 are holes in the valence band, Φ_{Bp} is the crucial interface electronic parameter, which determines the ease of transport of incoming electrons from the Fermi level of Mo to the valence band of p-MoS_2. For a Mo/n-MoS_2 metal-semiconductor junction, since the majority carriers in n-MoS_2 are electrons in the conduction band, Φ_{Bn} is the crucial interface electronic parameter, which determines the ease of transport of incoming electrons from the Fermi level of Mo to the conduction band of n-MoS_2. On the other hand, the ease of transport of holes from the valence band of p-MoS_2 to Mo metal is determined by the qV_o parameter.

3. Results and discussion

Mo/CZTS/CdS/i-ZnO/Al TFSC without any interfacial MoS_2 layer is set as a baseline case in this study. The photovoltaic performance parameters for this baseline configuration are $V_{oc} = 0.43$ V, $J_{sc} = 33.1$ mA/cm^2, FF = 78.7% and PCE = 11.2%. The obtained result is considerably lower than most of the simulated cases with MoS_2 interfacial layer primarily due to large work function of CZTS, $\Phi_{CZTS} > \Phi_{Mo}$, which results in high back contact barrier Φ_{Bp} of 1.21 eV and high contact potential qV_o of 1.14 eV. In the next few subsequent sub-sections, device performance and characteristics of CZTS TFSC with p and n- type MoS_2 with variable carrier concentration, layer thickness, χ, and E_g are discussed.

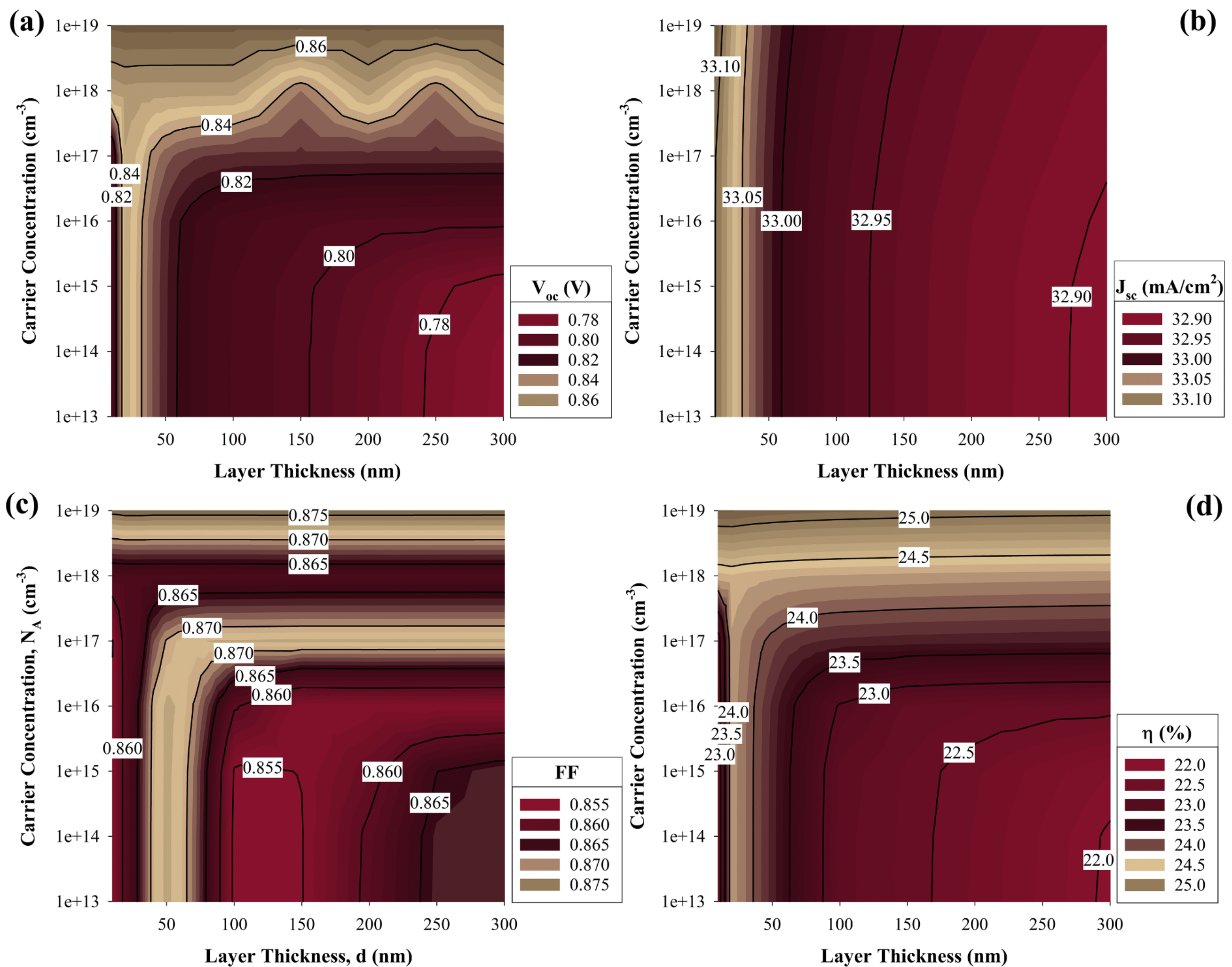

Fig. 1. Contour graphs of CZTS TFSC performance parameters dependency on p-MoS_2 carrier concentration and layer thickness variables.

(i) Effects of carrier concentration and layer thickness

Figs. 1 and 2 represent contour graphs of CZTS TFSCs performance parameters dependency on p and n-MoS_2 carrier concentration and layer thickness variables, respectively. The effect of carrier concentration from 10^{13} to 10^{19} cm^{-3} and thickness from 10 to 300 nm are probed to explore the device performance.

As shown, the graphs depict V_{oc} dependency on the variables of both types of MoS_2 layers demonstrate fairly contrasting results. The formation of p-MoS_2 results in higher V_{oc} with values ranging from 0.78 to 0.86 V. It is observed that the p-MoS_2 layer performs better in terms of V_{oc} at $N_A > 10^{17}$ cm^{-3} in the range of 10–100 nm and beyond this range, the N_A has to be preserved above 10^{18} cm^{-3} to maintain the maximum attainable V_{oc}. At $N_A < 10^{18}$ cm^{-3}, V_{oc} minutely decreases in either very thin layers below ~20 nm or more than ~40 nm. On the other hand, n-type MoS_2 results in inferior V_{oc} extending from 0.2 to 0.8 V in the investigated range (Fig. 2(a)). In contrast to p-MoS_2, a lower N_D is favorable in this case, and the increase in the thickness from 10 to 300 nm results V_{oc} of 0.7 V at the N_D of 10^{18} to 10^{16} cm^{-3}, respectively. The highest V_{oc} (~0.85 V) is obtained at $N_D < 10^{17}$ in the low range of thickness specially in the vicinity of ~20 nm. Variation in MoS_2 carrier concentration significantly affects the band alignment at the Mo/MoS_2 and MoS_2/CZTS junctions. Fig. 3 illustrates the equilibrium band alignments for Mo/MoS_2/CZTS structure for p and n-MoS_2 in monolayer and bulk configurations. The calculated interface and band alignment related electronic parameters for p-MoS_2 and n-MoS_2 in the investigated carrier concentration range are tabulated in Tables 2 and 3, respectively.

As can be noted, Φ_{Bn}, Φ_{Bp}, ΔE_c, and ΔE_v parameters are constant regardless of the variation in density of carrier concentration of p and n-MoS_2. Hence, the resulting device performance is solely a composite function of qV_o and $qV_{bi_{back}}$ parameters. Generally, for Mo/p-MoS_2/CZTS band alignment, lower negative $qV_{bi_{back}}$ or higher positive $qV_{bi_{back}}$ and lower qV_o are desirable for hole transport across valence band of CZTS to valence band of p-MoS_2 and from valence band of p-MoS_2 to Mo metal. Increase in N_A results in higher qV_o and lower negative $qV_{bi_{back}}$ parameters for p-type MoS_2 as shown in Table 2. Increase of N_A in p-MoS_2 results in comparatively beneficial band bending for both conduction band (E_c) and valence band (E_v) after the junction is formed. As the N_A increases, fermi level (E_f) shifts downwards resulting in increasing ease of hole flow from CZTS to MoS_2. It also increases electron flow inhibition from CZTS to MoS_2 and thus, reducing carrier recombination at back contact. Hence, higher N_A results in higher V_{oc} due to the favorable band alignment at the back contact. In contrast for n-MoS_2, higher N_d induced higher negative $qV_{bi_{back}}$ drives the minority carriers (electrons), which are photo-generated in n-MoS_2/CZTS junction towards back contact, thus resulting in enhanced electron current. The increased electron current contribution to the forward diode subsequently reduces the V_{oc} (Pan et al., 2006). As shown in Fig. 2(a) and inset (2) in Fig. 3, the decrement in V_{oc} is more pronounced for N_D greater than 10^{17} cm^{-3}.

The J_{sc} shows very insignificant variation for the different

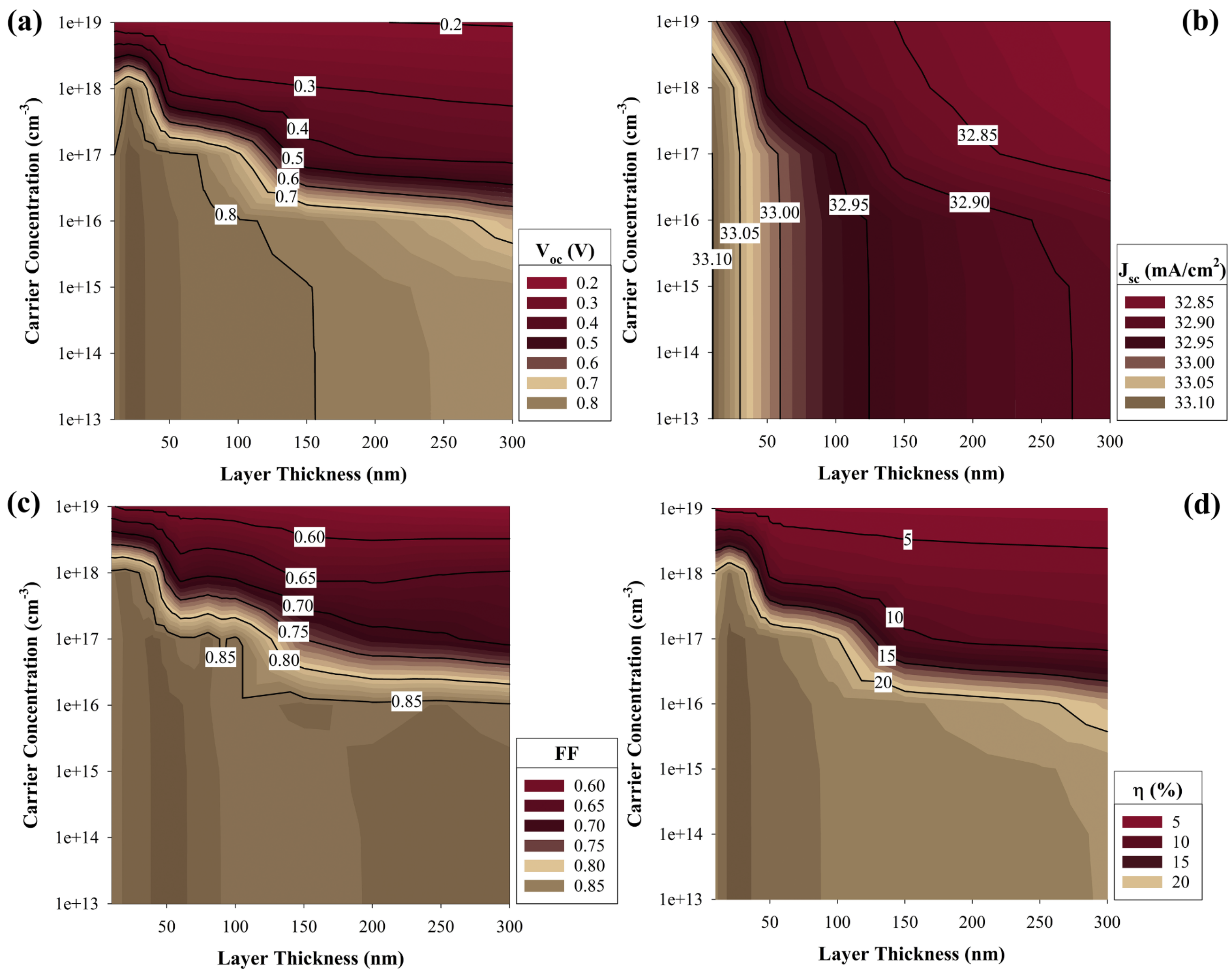

Fig. 2. Contour graphs of CZTS TFSC performance parameters dependency on n-MoS_2 carrier concentration and layer thickness variables.

combinations of carrier concentration and thickness for both cases of p and n-MoS_2 layers. The abrupt transition of J_{sc}, which was reported by Niemegeers et al. (1995) due to the absorber's properties, is not observed in this study. Even within the small changes in the J_{sc} values, the phenomenon of higher carrier concentration and lower thickness are preferred for p-type MoS_2 while lower values in both carrier concentration and thickness are desired for its counterpart. Generally, photocurrent is directly proportional to various factors for instance electric charge of electron, cross-sectional area of p-n heterojunction, generation rate of electron-hole pair, diffusion length of minority carriers in the p and n-side, and depletion width of the main p-absorber layer/n-buffer layer heterojunction (Hossain et al., 2018). These factors are not affected significantly in our simulation although, the J_{sc} follows the transition based on band alignment at the p-n heterojunctions.

Ideally, FF is only a function of V_{oc} (Green, 1981). However, basically FF does not only depend on the V_{oc} but also the recombination processes in the depletion region. Higher FF is observed for p-MoS_2 ranging from 0.855 to 0.875 compared to n-type MoS_2 ranging from 0.6 to 0.85. The overall trend is similar to the V_{oc} results. The only notable difference is observed in p-MoS_2 in which the highest range of FF is shifted towards ~40–60 nm thickness. Finally, PCE = $V_{oc} \times J_{sc} \times$ FF equation suggests that PCE is an amalgamation of the three output parameters discussed above and based on the significance of V_{oc} and FF variation in this study, an accustomed trend is observed. Lower performance for p-MoS_2 is found in both thicker and thinner layers at $N_A < 10^{17}$ cm^{-3} (right and left-bottom zone of contour plot), whereas for the n-MoS_2, lower N_D is preferred for higher device efficiency. Naturally, it is found that p-type MoS_2 is superior to n-type MoS_2 within the range of investigation. PCE varied from 22 to 25% for p-type whereas n-type ranged from 5 to 20%. As found, p-MoS_2 prefers higher N_A (> 10^{17} cm^{-3}) and n-type requires lower N_D (< 10^{16} cm^{-3}), independent of the layer thickness. Interestingly, at carrier concentration < 10^{17} cm^{-3}, the PCE for p- and n- MoS_2 layers is decreased slightly from thickness of ~20 to ~10 nm. This reduction becomes more substantial once the thickness of p- or n-MoS_2 reduced to 0.61 nm (monolayer thickness). Inclusion of monolayer p- or n-MoS_2 in CZTS TFSC results in zero PCE due to large values of E_g and χ, which in turn, forms high barrier height Φ_{Bp} and Φ_{Bn} of 1.75 eV. Consequently, we found that monolayer MoS_2 is very detrimental for CZTS TFSC due to unfavorable band alignment at the Mo/MoS_2 junction, although from practical point of view this drawback could be negated through carrier tunneling effect (Yang et al., 2015).

(ii) Effects of band gap and electron affinity

Based on the aforesaid results, variation in the E_g and χ are investigated at two significant domains of carrier concentration values of 10^{16} and 10^{18} cm^{-3} for both types of MoS_2 while the layer thickness is set 50 nm. In regards to Mo/MoS_2 metal-semiconductor junction and MoS_2/CZTS heterojunction, E_g and χ of both types of MoS_2 crucially determine Φ_{Bn}, Φ_{Bp}, ΔE_c, and ΔE_v as given in Eqs. (1) and (2) and (5) and (6). Consequently, the overall Mo/MoS_2/CZTS band alignment

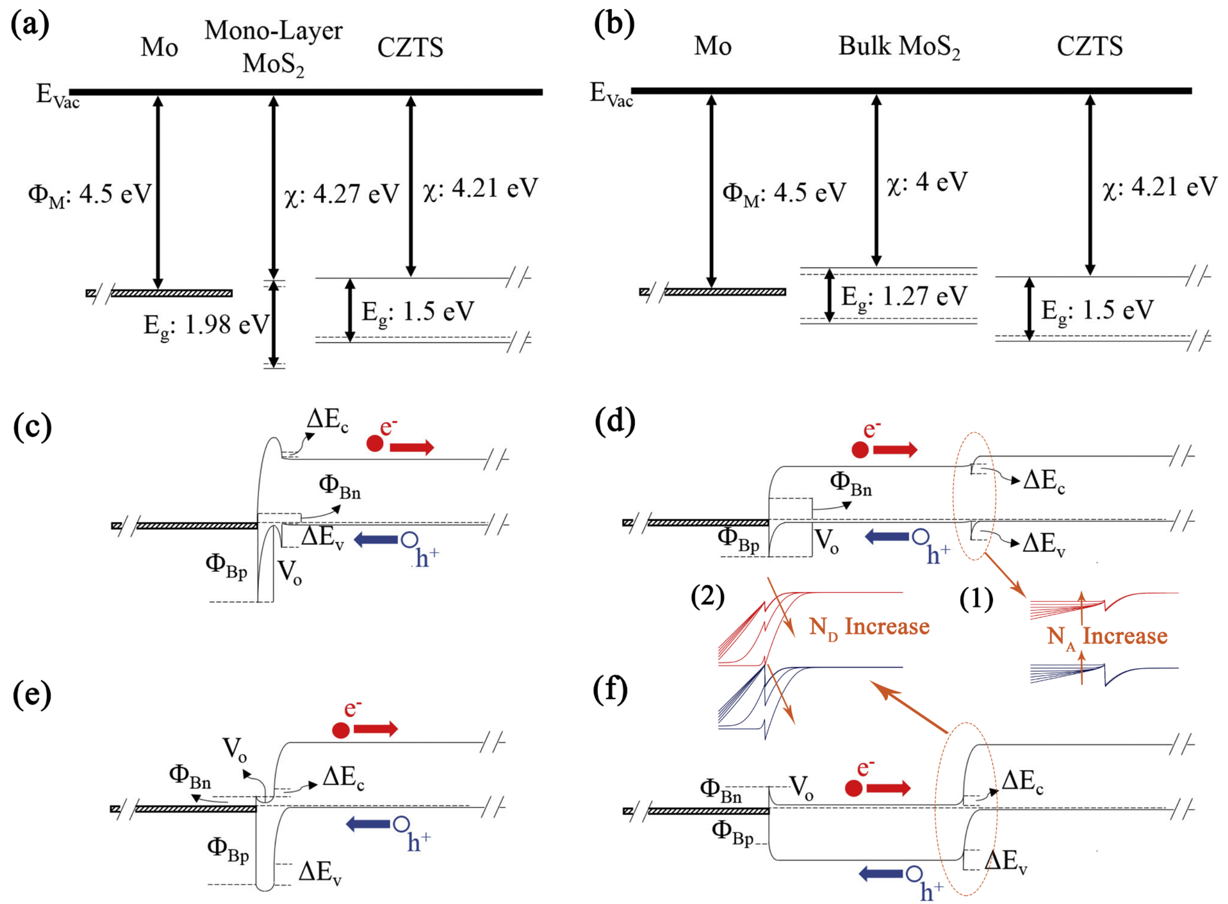

Fig. 3. Equilibrium band alignment of Mo/MoS_2/CZTS in various configurations (a) isolated monolayer MoS_2 (b) isolated bulk MoS_2 (c) Mo/monolayer p-MoS_2/CZTS (d) Mo/bulk p-MoS_2/CZTS (e) Mo/monolayer n-MoS_2/CZTS (f) Mo/bulk n-MoS_2/CZTS. Inset (1) and (2) represent the effects of carrier concentration in the MoS_2/CZTS band alignment obtained from simulation results.

Table 2
Calculated interface electronic parameters of Mo/p-MoS_2/CZTS for various N_A of mono-layer and bulk p-MoS_2.

Band Diagram Parameters (eV)		N_A (cm^{-3}) mono-layer p-MoS_2	N_A (cm^{-3}) bulk p-MoS_2						
		10^{13}–10^{19}	10^{13}	10^{14}	10^{15}	10^{16}	10^{17}	10^{18}	10^{19}
Mo/p-MoS_2	Φ_{Bn}	0.23	0.5	0.5	0.5	0.5	0.5	0.5	0.5
Mo/p-MoS_2	Φ_{Bp}	1.75	0.77	0.77	0.77	0.77	0.77	0.77	0.77
Mo/p-MoS_2	qV_o	1.37714–1.73478	0.39714	0.45675	0.51635	0.57596	0.63557	0.69518	0.75478
p-MoS_2/CZTS	ΔE_c	−0.06	0.21	0.21	0.21	0.21	0.21	0.21	0.21
p-MoS_2/CZTS	ΔE_v	0.54	−0.44	−0.44	−0.44	−0.44	−0.44	−0.44	−0.44
p-MoS_2/CZTS	$qV_{bi_{back}}$	0.24196–0.59961	−0.73804	−0.67843	−0.61882	−0.55921	−0.49961	−0.44000	−0.38039

Table 3
Calculated interface electronic parameters of Mo/n-MoS_2/CZTS for various N_D of mono-layer and bulk n-MoS_2.

Band Diagram Parameters (eV)		N_D (cm^{-3}) mono-layer n-MoS_2	N_D (cm^{-3}) Bulk n-MoS_2						
		10^{13}–10^{19}	10^{13}	10^{14}	10^{15}	10^{16}	10^{17}	10^{18}	10^{19}
Mo/n-MoS_2	Φ_{Bn}	0.23	0.5	0.5	0.5	0.5	0.5	0.5	0.5
Mo/n-MoS_2	Φ_{Bp}	1.75	0.77	0.77	0.77	0.77	0.77	0.77	0.77
Mo/n-MoS_2	qV_o	−0.08845 to 0.26920	0.18155	0.24116	0.30077	0.36037	0.41998	0.47959	0.53920
n-MoS_2/CZTS	ΔE_c	−0.06	0.21	0.21	0.21	0.21	0.21	0.21	0.21
n-MoS_2/CZTS	ΔE_v	0.54	−0.44	−0.44	−0.44	−0.44	−0.44	−0.44	−0.44
n-MoS_2/CZTS	$qV_{bi_{back}}$	−1.04673 to −1.40437	−1.31673	−1.37634	−1.43594	−1.49555	−1.55516	−1.61477	−1.67437

changes with variation of E_g and χ, which subsequently effects on the overall performance of CZTS TFSCs. The effects of variable χ and E_g of MoS_2 on the CZTS TFSC performance are shown in Fig. 4. As shown, both CZTS devices with n-MoS_2 and p-MoS_2 with carrier concentration of 10^{16} cm^{-3} show similar and almost identical linearly decreasing PCE from 25% to 5% with the increase in χ and E_g. The lack of distinguished outcome is due the default thickness of 50 nm and a moderate doping level of 10^{16} cm^{-3} used for these simulations. It is observed that only at

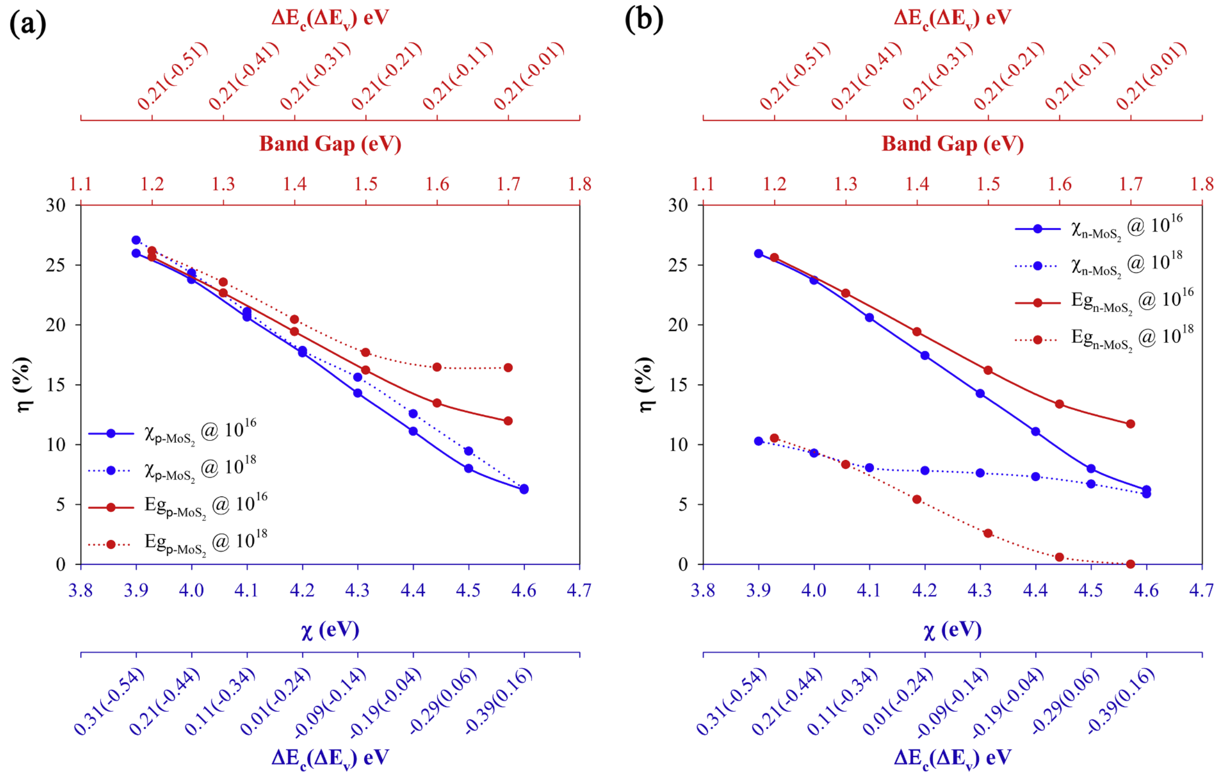

Fig. 4. Effects of χ and E_g on the PCE of CZTS TFSC with MoS_2 interfacial layer with carrier concentration of 10^{16} and 10^{18} cm^{-3} (a) p-type (b) n-type.

higher doping levels, the two different conductivity types demonstrate distinguishing phenomenon whereby the device with n-MoS_2 layer with higher carrier concentration of 10^{18} cm^{-3} exhibits comparatively low PCE at lower values of χ and E_g as depicted in Fig. 4. At this carrier concentration, n-MoS_2 with E_g of 1.55 eV and above results in non-working device (PCE of 0%).

Fig. 5 illustrates the equilibrium band alignments for Mo/MoS_2/CZTS structure for p and n-MoS_2 with variable χ and E_g values. The calculated interface and band alignment related electronic parameters for p and n-MoS_2 in the investigated variable χ and E_g values range are tabulated in Tables 4–7, respectively.

Variation in χ shifts the whole band structure of a material upward or downward as shown in Fig. 5. This in turn has effect on ΔE_c and ΔE_v of the MoS_2/CZTS heterojunction and Φ_{Bp}, Φ_{Bn} and qV_o of the Mo/MoS_2 metal-semiconductor junction (Sze and Ng, 2006). For instance, MoS_2 with χ of 4.6 eV has ΔE_c and ΔE_v of -0.39 eV and 0.16 eV, respectively whereas χ of 3.9 eV creates 0.31 eV and -0.54 eV as well as the resulting changes in Φ_{Bp}, Φ_{Bn} and qV_o as shown in the Tables 4 and 5. For the n-MoS_2 which forms anisotype heterojunction with p-CZTS, lower values of χ results in positive ΔE_c, which suggest limited electron flow from the lower energy conduction band of CZTS to the higher energy conduction band of MoS_2. This phenomenon is beneficial as inhibition of electron flow towards the back contact is desired. On the other hand, higher χ results in negative ΔE_c indicating spontaneous electron flow from the higher energy conduction band of CZTS to the lower energy conduction band of MoS_2. This affects the device performance as electron flow towards the back contact could result in recombination of charge carriers. This effect of charge carrier recombination is exaggerated when population of electron increases due to the alteration of doping concentration from 10^{16} cm^{-3} to 10^{18} cm^{-3} as observed. The transition of ΔE_v value from positive to negative with lowering of χ also suggests the ease of hole flow from CZTS to back contact through MoS_2. This supports the results obtained from simulations as observed in Fig. 4. On the other hand, for the p-MoS_2, lower χ yields negative ΔE_v indicating ease of hole flow from the higher energy valence band of CZTS to the lower energy valence band of MoS_2. The intended direction of hole flow during charge carrier separation is towards back contact. Higher χ provides the positive ΔE_v, which corresponds to an energy barrier for the lower energy holes of CZTS towards the MoS_2. This inhibition of hole flow towards back contact is undesired and detrimental for effective carrier collection. This hole barrier phenomenon has been observed in earlier works (Dhakal et al., 2015). The effect of hole barrier can be overcome slightly by increasing overall hole population through doping increase from 10^{16} to 10^{18} cm^{-3} which is observed by the slight improvement in the device performance as seen in Fig. 4. The significant difference in device performance due to variation in doping level is observed for n-MoS_2 compared to the p-MoS_2, which can be explained from the perspective of isotype/anisotype junction that they form with CZTS layer. When the majority and minority carriers are same in adjacent layers of p-CZTS and p-MoS_2 with an isotype junction, the effect of N_A is not that drastic when compared to anisotype junction between p-CZTS and n-MoS_2 where majority and minority carriers in adjacent layer are different and any modest change in doping level > 10^{16} cm^{-3} can have a huge impact on the carrier flow and device performance. This is due to the magnitude of the $qV_{bi_{back}}$ of the MoS_2/CZTS heterojunction as tabulated in Tables 4 and 5. The n-MoS_2 generally forms back diode with higher negative $qV_{bi_{back}}$ compared to p-MoS_2, which is in turn, inhibits the hole transport from the CZTS layer to the MoS_2 layer. Although, positive $qV_{bi_{back}}$ has been observed for p-MoS_2 with high χ of 4.6 eV, which is supposedly to act as a beneficial back surface field, degradation PCE is still observed due to the positive ΔE_v and high Φ_{Bp} and qV_o value. High Φ_{Bp} and qV_o are responsible for inhibition of hole transport from the p-MoS_2 to the Mo back contact which stems from the variation in χ of MoS_2. Given a fixed doping profile and E_g, change in χ means change in work function. For an n-MoS_2/Mo junction, $\Phi_m > \Phi_n$ results in rectifying contact. Given a Φ_m of 4.5 eV, any $\Phi_n < 4.5$ eV yields a rectifying contact. For a moderate doping of 10^{16} cm^{-3} and E_g of 1.27 eV, any $\chi < 4.38$ eV would result in rectifying contact. As the Φ_n becomes higher with increasing χ, the junction goes through a transition from

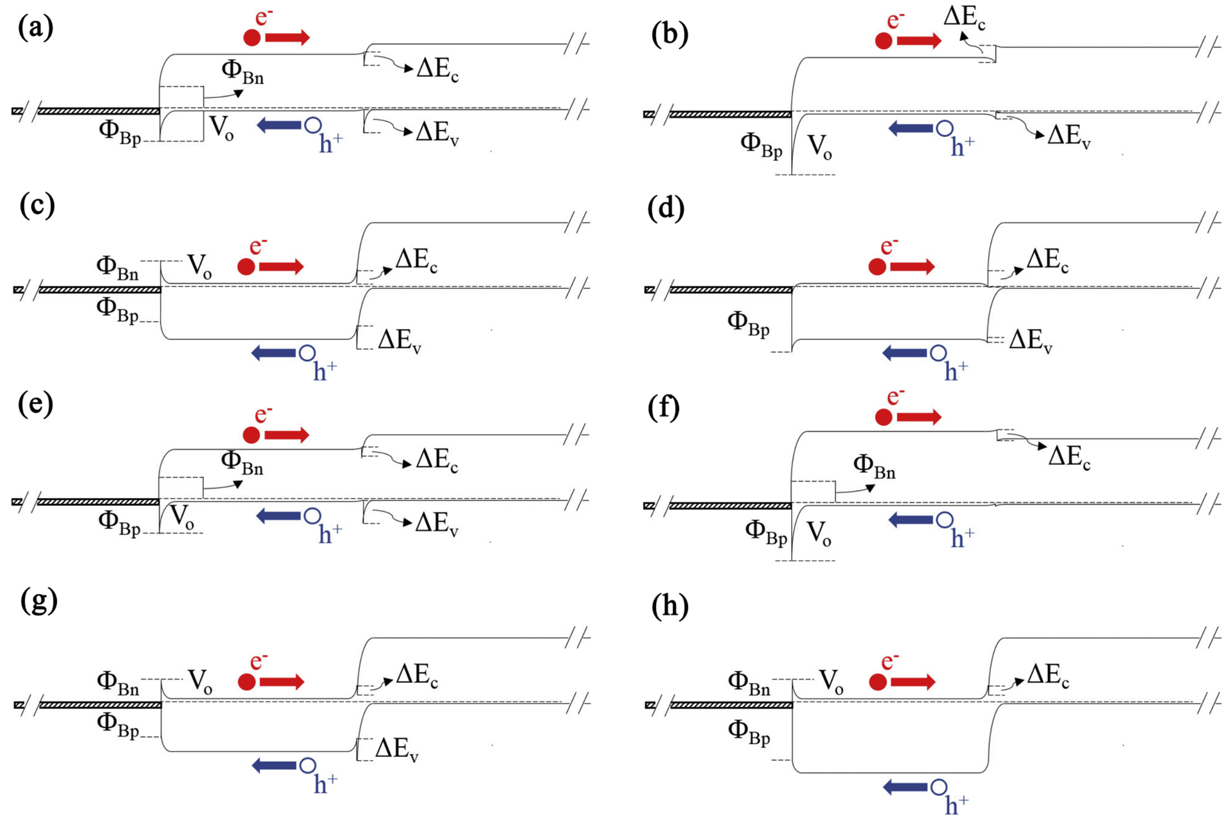

Fig. 5. Equilibrium band alignment of $Mo/MoS_2/CZTS$ in various χ and E_g of MoS_2 (a) bulk p-MoS_2 at χ of 3.9 eV (b) bulk p-MoS_2 at χ of 4.6 eV (c) bulk n-MoS_2 at χ of 3.9 eV (d) bulk n-MoS_2 at χ of 4.6 eV (e) bulk p-MoS_2 at E_g of 1.2 eV (f) bulk p-MoS_2 at E_g of 1.7 eV (g) bulk n-MoS_2 at E_g of 1.2 eV (h) bulk n-MoS_2 at E_g of 1.7 eV.

rectifying to ohmic. Owing to increasing ease of electron flow towards ohmic back contact due to the negative $qV_{bi_{back}}$, the performance goes down as evident from the simulation result. Furthermore, for n-MoS_2 with χ higher than 4.38 eV, qV_o becomes negative indicating that the photo-generated electron in the vicinity of Mo/n-MoS_2 can readily diffuse into Mo metal due to the absence of retarding potetnial barrier (positive qV_o). Whereas, for a p-MoS_2/Mo junction, $\Phi_m < \Phi_p$ yields a rectifying contact which is undesired in case of hole flow. Any χ more than 3.4 eV forms a rectifying contact. So, p-MoS_2 always forms a rectifying contact with Mo in our investigated range (3.9–4.6 eV) of χ. However, the trend of degrading performance with higher χ was also observed for p-MoS_2/Mo junction due to the fact that Φ_{Bp} and qV_o increases with the increase in χ. Given a fixed carrier concentration and thickness, this increase in Φ_{Bp} and qV_o results in further obstruction of hole flow towards back contact resulting in inferior PCE.

Calculated interface electronic parameters due to the variation in the E_g of MoS_2 are shown in Tables 6 and 7. Change in E_g usually translates in simultaneous change in E_c, E_v, and E_f. Increase in E_g can be seen as upshifting of E_c and/or downshifting of E_v and appropriate shifting of E_f according to the type of doping. In this study, increase in E_g of MoS_2 is assumed to be due to downshifting of E_v due to the constant χ. Therefore, increase in E_g does not change the E_c and E_{fn} of n-MoS_2 hence resulting in constant $qV_{bi_{back}}$. As seen, n-MoS_2 is already detrimental as it forms a back diode with p-CZTS which opposes the working built-in potential of p-CZTS/n-CdS primary diode. However, $qV_{bi_{back}}$ can be further exacerbated by increasing doping level that can upshift E_{fn} even higher close to conduction band. Moreover, with increasing E_g, even bigger detrimental effect of higher ΔE_v is induced because, hole as majority carrier carries more significance towards back contact. As E_g goes higher, E_v shifts lower and increasing positive value

Table 4
Calculated interface electronic parameters of Mo/bulk p-MoS_2/CZTS for various χ of p-MoS_2.

Band Diagram Parameters (eV)		χ (eV)								
		3.9	3.9	4	4.1	4.2	4.3	4.4	4.5	4.6
N_A: 10^{16} cm^{-3}	Mo/p-MoS_2	Φ_{Bn}	0.6	0.5	0.4	0.3	0.2	0.1	0	−0.1
	Mo/p-MoS_2	Φ_{Bp}	0.67	0.77	0.87	0.97	1.07	1.17	1.27	1.37
	Mo/p-MoS_2	qV_o	0.53037	0.63037	0.73037	0.83037	0.93037	1.03037	1.13037	1.23037
	p-MoS_2/CZTS	ΔE_c	0.31	0.21	0.11	0.01	−0.09	−0.19	−0.29	−0.39
	p-MoS_2/CZTS	ΔE_v	−0.54	−0.44	−0.34	−0.24	−0.14	−0.04	0.06	0.16
	p-MoS_2/CZTS	$qV_{bi_{back}}$	−0.60480	−0.50480	−0.40480	−0.30480	−0.20480	−0.10480	−0.00480	0.09520
N_A: 10^{18} cm^{-3}	Mo/p-MoS_2	Φ_{Bn}	0.6	0.5	0.4	0.3	0.2	0.1	0	−0.1
	Mo/p-MoS_2	Φ_{Bp}	0.67	0.77	0.87	0.97	1.07	1.17	1.27	1.37
	Mo/p-MoS_2	qV_o	0.64959	0.74959	0.84959	0.94959	1.04959	1.14959	1.24959	1.34959
	p-MoS_2/CZTS	ΔE_c	0.31	0.21	0.11	0.01	−0.09	−0.19	−0.29	−0.39
	p-MoS_2/CZTS	ΔE_v	−0.54	−0.44	−0.34	−0.24	−0.14	−0.04	0.06	0.16
	p-MoS_2/CZTS	$qV_{bi_{back}}$	−0.48559	−0.38559	−0.28559	−0.18559	−0.08559	0.01441	0.11441	0.21441

Table 5
Calculated interface electronic parameters of Mo/bulk n-MoS_2/CZTS for various χ of n-MoS_2.

Band Diagram Parameters (eV)			χ (eV)							
			3.9	4	4.1	4.2	4.3	4.4	4.5	4.6
N_D: 10^{16} cm^{-3}	Mo/n-MoS_2	Φ_{Bn}	0.6	0.5	0.4	0.3	0.2	0.1	0	−0.1
	Mo/n-MoS_2	Φ_{Bp}	0.67	0.77	0.87	0.97	1.07	1.17	1.27	1.37
	Mo/n-MoS_2	qV_o	0.46037	0.36037	0.26037	0.16037	0.06037	−0.03963	−0.13963	−0.23963
	n-MoS_2/CZTS	ΔE_c	0.31	0.21	0.11	0.01	−0.09	−0.19	−0.29	−0.39
	n-MoS_2/CZTS	ΔE_v	−0.54	−0.44	−0.34	−0.24	−0.14	−0.04	0.06	0.16
	n-MoS_2/CZTS	$qV_{bi_{back}}$	−1.59555	−1.49555	−1.39555	−1.29555	−1.19555	−1.09555	−0.99555	−0.89555
N_D: 10^{18} cm^{-3}	Mo/n-MoS_2	Φ_{Bn}	0.6	0.5	0.4	0.3	0.2	0.1	0	−0.1
	Mo/n-MoS_2	Φ_{Bp}	0.67	0.77	0.87	0.97	1.07	1.17	1.27	1.37
	Mo/n-MoS_2	qV_o	0.57959	0.47959	0.37959	0.27959	0.17959	0.07959	−0.02041	−0.12041
	n-MoS_2/CZTS	ΔE_c	0.31	0.21	0.11	0.01	−0.09	−0.19	−0.29	−0.39
	n-MoS_2/CZTS	ΔE_v	−0.54	−0.44	−0.34	−0.24	−0.14	−0.04	0.06	0.16
	n-MoS_2/CZTS	$qV_{bi_{back}}$	−1.71477	−1.61477	−1.51477	−1.41477	−1.31477	−1.21477	−1.11477	−1.01477

of ΔE_v, which prohibits hole flow from CZTS to MoS_2 towards the back contact. These too correlate with results from Fig. 4 and existing literature (Seo et al., 2014). Change E_g usually has similar effect for a p-MoS_2 as its n counter type. A p-MoS_2 has isotype junction with p-CZTS. A p-MoS_2 has the added advantage of having the back diode condition lesser negative values, resulting in slightly better performance. The magnitude of the effect of doping level varies with the conductivity type of MoS_2 layer due alteration in heterojunction type as discussed in earlier section. Change in E_g doesn't seem to have direct effect on Mo/n-MoS_2 junction owing to the unchanging conduction band energy level of n-MoS_2. The overall decrease in performance with increase in E_g may have been mainly due to adverse n-MoS_2/CZTS junction as discussed before. For a Mo/p-MoS_2 junction, increase in MoS_2 E_g can translate into increase in work function due to the possible downshift in E_v and E_{fp}. This results in increase in Φ_{Bp} and qV_o with increasing E_g, which compounds the inhibition of hole flow to the back contact. However, increased hole population by higher doping (from 10^{16} cm^{-3} to 10^{18} cm^{-3}) can yield slightly better performance for p-MoS_2 with higher E_g as observed from Fig. 4 due to the comparatively beneficial lower negative $qV_{bi_{back}}$ of the p-MoS_2/CZTS heterojunction.

4. Conclusions

This numerical study demonstrates effect of both n-type MoS_2 and p-type MoS_2 with varying material properties on the performance of a kesterite CZTS thin film solar cell. Numerical simulations were performed to analyse the dependence of the TFSC output parameters such as J_{sc}, V_{oc}, FF, and PCE to a wide range of thickness, carrier concentration, E_g and χ of both possible types of MoS_2 that can be formed between CZTS absorber and back contact. From this study it was found that formation of MoS_2 interfacial layer largely improves the performance of CZTS TFSC compared to device without any MoS_2 layer. This is due to the lower back contact barrier formation between Mo/MoS_2 associated to Mo/CZTS, regardless of the MoS_2 conductivity type. It was identified that the p-type MoS_2 with E_g of 1.2 eV and high carrier concentration of 10^{18} cm^{-3} can be beneficial for the CZTS TFSC in contrast to an n-type MoS_2 that can have an adverse effect on overall performance as a direct result of the n-p-n structure. It was also shown that the n-MoS_2 layer needs to be very thin with $N_D < 10^{17}$ cm^{-3} in order to be effective or operational. On the other hand, MoS_2 with lower χ and E_g values of 3.9 eV and 1.2 eV are desirable for both p and n-type MoS_2 due to favourable band alignment condition especially CBO and VBO. This study shows the prospect of p-type MoS_2 as a beneficial back contact buffer layer. It also provides a limiting condition for n-MoS_2 if formation of n-MoS_2 is absolutely unavoidable. Thus, this analysis might be a promising approach towards managing interfacial MoS_2 layer in CZTS TFSCs and ultimately achieving higher energy conversion efficiencies.

Table 6
Calculated interface electronic parameters of Mo/bulk p-MoS_2/CZTS in various E_g of p-MoS_2.

Band Diagram Parameters (eV)			E_g (eV)					
			1.2	1.3	1.4	1.5	1.6	1.7
N_A: 10^{16} cm^{-3}	Mo/p-MoS_2	Φ_{Bn}	0.5	0.5	0.5	0.5	0.5	0.5
	Mo/p-MoS_2	Φ_{Bp}	0.7	0.8	0.9	1	1.1	1.2
	Mo/p-MoS_2	qV_o	0.56037	0.66037	0.76037	0.86037	0.96037	1.06037
	p-MoS_2/CZTS	ΔE_c	0.21	0.21	0.21	0.21	0.21	0.21
	p-MoS_2/CZTS	ΔE_v	−0.51	−0.41	−0.31	−0.21	−0.11	−0.01
	p-MoS_2/CZTS	$qV_{bi_{back}}$	−0.57480	−0.47480	−0.37480	−0.27480	−0.17480	−0.07480
N_A: 10^{18} cm^{-3}	Mo/p-MoS_2	Φ_{Bn}	0.5	0.5	0.5	0.5	0.5	0.5
	Mo/p-MoS_2	Φ_{Bp}	0.7	0.8	0.9	1	1.1	1.2
	Mo/p-MoS_2	qV_o	0.67959	0.77959	0.87959	0.97959	1.07959	1.17959
	p-MoS_2/CZTS	ΔE_c	0.21	0.21	0.21	0.21	0.21	0.21
	p-MoS_2/CZTS	ΔE_v	−0.51	−0.41	−0.31	−0.21	−0.11	−0.01
	p-MoS_2/CZTS	$qV_{bi_{back}}$	−0.45559	−0.35559	−0.25559	−0.15559	−0.05559	0.04441

Table 7
Calculated interface electronic parameters of Mo/bulk n-MoS_2/CZTS in various E_g of n-MoS_2.

Band Diagram Parameters (eV)			E_g (eV)					
			1.2	1.3	1.4	1.5	1.6	1.7
N_D: 10^{16} cm^{-3}	Mo/n-MoS_2	Φ_{Bn}	0.5	0.5	0.5	0.5	0.5	0.5
	Mo/n-MoS_2	Φ_{Bp}	0.7	0.8	0.9	1	1.1	1.2
	Mo/n-MoS_2	qV_o	0.36037	0.36037	0.36037	0.36037	0.36037	0.36037
	n-MoS_2/CZTS	ΔE_c	0.21	0.21	0.21	0.21	0.21	0.21
	n-MoS_2/CZTS	ΔE_v	−0.51	−0.41	−0.31	−0.21	−0.11	−0.01
	n-MoS_2/CZTS	$qV_{bi_{back}}$	−1.49555	−1.49555	−1.49555	−1.49555	−1.49555	−1.49555
N_D: 10^{18} cm^{-3}	Mo/n-MoS_2	Φ_{Bn}	0.5	0.5	0.5	0.5	0.5	0.5
	Mo/n-MoS_2	Φ_{Bp}	0.7	0.8	0.9	1	1.1	1.2
	Mo/n-MoS_2	qV_o	0.47959	0.47959	0.47959	0.47959	0.47959	0.47959
	n-MoS_2/CZTS	ΔE_c	0.21	0.21	0.21	0.21	0.21	0.21
	n-MoS_2/CZTS	ΔE_v	−0.51	−0.41	−0.31	−0.21	−0.11	−0.01
	n-MoS_2/CZTS	$qV_{bi_{back}}$	−1.61477	−1.61477	−1.61477	−1.61477	−1.61477	−1.61477

Acknowledgments

The authors would like to acknowledge Universiti Kebangsaan Malaysia through NPRP grant # [RS-2015-001] awarded by Qatar National Research Fund (a member of Qatar Foundation). The authors would also like to acknowledge Institute of Sustainable Energy (ISE) of Universiti Tenaga Nasional (@The National Energy University) for their cordial support through BOLD2025 Program. The findings achieved herein are solely the responsibility of the authors.

References

Abou-Ras, D., Kostorz, G., Bremaud, D., Kälin, M., Kurdesau, F.V., Tiwari, A.N., Döbeli, M., 2005. Formation and characterisation of $MoSe_2$ for Cu(In, Ga)Se_2 based solar cells. Thin Solid Films 480–481, 433–438.

Amin, N., Hossain, M.I., Chelvanathan, P., Uzzaman, A.S.M.M., Sopian, K., 2010. Prospects of Cu2ZnSnS4 (CZTS) solar cells from numerical analysis. In: International Conference on Electrical & Computer Engineering (ICECE 2010), pp. 730–733.

Anderson, R.L., 1960. Germanium-gallium arsenide heterojunctions [Letter to the Editor]. IBM J. Res. Develop. 4 (3), 283–287.

Brahim, A., Ruth, P., Shin, M., 2016. Theoretical analysis of the combined effects of sulfur vacancies and analyte adsorption on the electronic properties of single-layer MoS_2. Nanotechnology 27 (18), 185701.

Chelvanathan, P., Shahahmadi, S.A., Arith, F., Sobayel, K., Aktharuzzaman, M., Sopian, K., Alharbi, F.H., Tabet, N., Amin, N., 2017. Effects of RF magnetron sputtering deposition process parameters on the properties of molybdenum thin films. Thin Solid Films 638, 213–219.

Chelvanathan, P., Shahahmadi, S.A., Ferdaous, M.T., Sapeli, M.M.I., Sopian, K., Amin, N., 2018. Controllable formation of MoS_2 via preferred crystallographic orientation modulation of DC-sputtered Mo thin film. Mater. Lett. 219, 174–177.

Chen, H.J., Fu, S.W., Wu, S.H., Tsai, T.C., Wu, H.T., Shih, C.F., 2016. Impact of SnS buffer layer at Mo/Cu_2ZnSnS_4 interface. J. Am. Ceram. Soc. 99 (5), 1808–1814.

Chow, P.K., Jacobs-Gedrim, R.B., Gao, J., Lu, T.-M., Yu, B., Terrones, H., Koratkar, N., 2015. Defect-induced photoluminescence in monolayer semiconducting transition metal dichalcogenides. ACS Nano 9 (2), 1520–1527.

Cozza, D., Ruiz, C.M., Duché, D., Simon, J.J., Escoubas, L., 2016. Modeling the back contact of $Cu_2ZnSnSe_4$solar cells. IEEE J. Photovolt. 6 (5), 1292–1297.

Cui, X., Lee, G.-H., Kim, Y.D., Arefe, G., Huang, P.Y., Lee, C.-H., Chenet, D.A., Zhang, X., Wang, L., Ye, F., Pizzocchero, F., Jessen, B.S., Watanabe, K., Taniguchi, T., Muller, D.A., Low, T., Kim, P., Hone, J., 2015. Multi-terminal transport measurements of MoS_2 using a van der Waals heterostructure device platform. Nat. Nanotechnol. 10, 534.

Cui, H., Liu, X., Song, N., Li, N., Liu, F., Hao, X., 2014. Impact of rapid thermal annealing of Mo coated soda lime glass substrate on device performance of evaporated Cu_2ZnSnS_4 thin film solar cells. Mater. Lett. 125, 40–43.

Daniele, C., Inge, A., Surajit, S., Serena, I., Valeri, A.E., Andre, S., Yashwanth, B., Lisanne, P., Markus, H., Manuel, M., Wilfried, V., Safak, S., Cedric, H., Matty, C., Marc, H., Stefan, D.G., Iuliana, R., Aaron, T., 2016. Controlled sulfurization process for the synthesis of large area MoS2 films and MoS_2/WS2 heterostructures. Adv. Mater. Interfaces 3 (4), 1500635.

Dashora, A., Ahuja, U., Venugopalan, K., 2013. Electronic and optical properties of MoS2 (0001) thin films: feasibility for solar cells. Comput. Mater. Sci. 69, 216–221.

Dhakal, T.P., Harvey, S., Hest, M.V., Teeter, G., 2015. Back contact band offset study of Mo-CZTS based solar cell structure by using XPS/UPS techniques. In: 2015 IEEE 42nd Photovoltaic Specialist Conference (PVSC), pp. 1–4.

Dileep, K., Sahu, R., Sarkar, S., Peter, S.C., Datta, R., 2016. Layer specific optical band gap measurement at nanoscale in MoS_2 and ReS_2 van der Waals compounds by high resolution electron energy loss spectroscopy. J. Appl. Phys. 119 (11), 114309.

Frisk, C., Ericson, T., Li, S.Y., Szaniawski, P., Olsson, J., Platzer-Björkman, C., 2016. Combining strong interface recombination with bandgap narrowing and short diffusion length in Cu_2ZnSnS_4 device modeling. Solar Energy Mater. Solar Cells 144, 364–370.

Gong, C., Zhang, H., Wang, W., Colombo, L., Wallace, R.M., Cho, K., 2013. Band alignment of two-dimensional transition metal dichalcogenides: Application in tunnel field effect transistors. Appl. Phys. Lett. 103 (5), 053513.

Green, M.A., 1981. Solar cell fill factors-general graph and empirical expressions. Solid State Electron. 24, 788.

Green, Martin A., Hishikawa, Yoshihiro, Dunlop, Ewan D., Levi, Dean H., Hohl-Ebinger, Jochen, Ho-Baillie, Anita W.Y., 2018. Solar cell efficiency tables (version 52). Progr. Photovolt.: Res. Appl. 26 (7), 427–436.

Hossain, E.S., Chelvanathan, P., Shahahmadi, S.A., Sopian, K., Bais, B., Amin, N., 2018. Performance assessment of Cu2SnS3 (CTS) based thin film solar cells by AMPS-1D. Curr. Appl. Phys. 18 (1), 79–89.

Hossain, M.I., Chelvanathan, P., Alam, M.M., Akhtaruzzaman, M., Sopian, K., Amin, N., 2013. Potential buffer layers for Cu2ZnSnS4 (CZTS) solar cells from numerical analysis. In: 2013 IEEE Conference on Clean Energy and Technology (CEAT), pp. 450–454.

Howell, S.L., Jariwala, D., Wu, C.-C., Chen, K.-S., Sangwan, V.K., Kang, J., Marks, T.J., Hersam, M.C., Lauhon, L.J., 2015. Investigation of band-offsets at monolayer-multilayer MoS2 junctions by scanning photocurrent microscopy. Nano Lett. 15 (4), 2278–2284.

Kang, J., Tongay, S., Zhou, J., Li, J., Wu, J., 2013. Band offsets and heterostructures of two-dimensional semiconductors. Appl. Phys. Lett. 102 (1), 012111.

Kappera, R., Voiry, D., Yalcin, S.E., Branch, B., Gupta, G., Mohite, A.D., Chhowalla, M., 2014. Phase-engineered low-resistance contacts for ultrathin MoS2 transistors. Nat. Mater. 13, 1128.

Katagiri, H., 2005. Cu_2ZnSnS_4 thin film solar cells. Thin Solid Films 480–481, 426–432.

Komsa, H.-P., Krasheninnikov, A.V., 2015. Native defects in bulk and monolayer MoS_2 from first principles. Phys. Rev. B 91 (12), 125304.

Laskar, M.R., Nath, D.N., Ma, L., Lee, E.W., Lee, C.H., Kent, T., Yang, Z., Mishra, R., Roldan, M.A., Idrobo, J.C., Pantelides, S.T., 2014. p-type doping of MoS2 thin films using Nb. Appl. Phys. Lett. 104 (9), 092104.

Li, W., Chen, J., Cui, H., Liu, F., Hao, X., 2014. Inhibiting MoS_2 formation by introducing a ZnO intermediate layer for Cu_2ZnSnS_4 solar cells. Mater. Lett. 130, 87–90.

Liu, F., Huang, J., Sun, K., Yan, C., Shen, Y., Park, J., Pu, A., Zhou, F., Liu, X., Stride, J.A., Green, M.A., Hao, X., 2017. Beyond 8% ultrathin kesterite Cu_2ZnSnS_4 solar cells by interface reaction route controlling and self-organized nanopattern at the back contact. Npg Asia Mater. 9, e401.

Neal, A.T., Pachter, R., Mou, S., 2017. P-type conduction in two-dimensional MoS_2 via oxygen incorporation. Appl. Phys. Lett. 110 (19), 193103.

Niemegeers, A., Burgelman, M., De Vos, A., 1995. On the CdS/$CuInSe_2$ conduction band discontinuity. Appl. Phys. Lett. 67 (6), 843–845.

Nipane, A., Karmakar, D., Kaushik, N., Karande, S., Lodha, S., 2016. Few-layer MoS2 p-type devices enabled by selective doping using low energy phosphorus implantation. ACS Nano 10 (2), 2128–2137.

Pan, J., Gloeckler, M., Sites, J.R., 2006. Hole current impedance and electron current enhancement by back-contact barriers in CdTe thin film solar cells. J. Appl. Phys. 100 (12), 124505.

Puvaneswaran, C., Mohammad Istiaque, H., Jamilah, H., Mohammad, A., Kamaruzzaman, S., Nowshad, A., 2012. Effects of transition metal dichalcogenide molybdenum disulfide layer formation in copper–zinc–tin–sulfur solar cells from numerical analysis. Jpn. J. Appl. Phys. 51 (10S), 10NC32.

Qiu, H., Pan, L., Yao, Z., Li, J., Shi, Y., Wang, X., 2012. Electrical characterization of back-gated bi-layer MoS2 field-effect transistors and the effect of ambient on their performances. Appl. Phys. Lett. 100 (12), 123104.

Reale, F., Sharda, K., Mattevi, C., 2016. From bulk crystals to atomically thin layers of group VI-transition metal dichalcogenides vapour phase synthesis. Appl. Mater. Today 3, 11–22.

Santos, E.J.G., Kaxiras, E., 2013. Electrically driven tuning of the dielectric constant in MoS2 layers. ACS Nano 7 (12), 10741–10746.

Schlaf, R., Lang, O., Pettenkofer, C., Jaegermann, W., 1999. Band lineup of layered semiconductor heterointerfaces prepared by van der Waals epitaxy: charge transfer

correction term for the electron affinity rule. J. Appl. Phys. 85 (5), 2732–2753.

Scragg, J.J., Wätjen, J.T., Edoff, M., Ericson, T., Kubart, T., Platzer-Björkman, C., 2012. A detrimental reaction at the molybdenum back contact in $Cu_2ZnSn(S, Se)_4$ thin-film solar cells. J. Am. Chem. Soc. 134 (47), 19330–19333.

Seo, D., Kim, C., Oh, E., Hong, C.W., Kim, J.H., Lim, S., 2014. Control of metal salt ratio and MoS_2 layer thickness in a Cu_2ZnSnS_4 thin film solar cell. J. Mater. Sci.: Mater. Electron. 25 (8), 3420–3426.

Shahahmadi, S.A., Yeganeh, B., Huda, N., Asim, N., Hafidz, M., Alam, M.M., AlOthman, Z.A., Sopian, K., Amin, N., 2015. Properties of a-SiGe thin films on glass by co-sputtering for photovoltaic absorber application. J. Nanosci. Nanotechnol. 15 (11), 9275–9280.

Suh, J., Park, T.-E., Lin, D.-Y., Fu, D., Park, J., Jung, H.J., Chen, Y., Ko, C., Jang, C., Sun, Y., Sinclair, R., Chang, J., Tongay, S., Wu, J., 2014. Doping against the native propensity of MoS_2: degenerate hole doping by cation substitution. Nano Lett. 14 (12), 6976–6982.

Sun, K., Yan, C., Liu, F., Huang, J., Zhou, F., Stride, J.A., Green, M., Hao, X., 2016. Over 9% efficient Kesterite Cu_2ZnSnS_4 solar cell fabricated by using $Zn_{1-x}Cd_xS$ buffer layer. Adv. Energy Mater. 6 (12), 1600046.

Sze, S.M., Ng, K.K., 2006. Physics of Semiconductor Devices. John Wiley & Sons.

Tongay, S., Suh, J., Ataca, C., Fan, W., Luce, A., Kang, J.S., Liu, J., Ko, C., Raghunathanan, R., Zhou, J., Ogletree, F., Li, J., Grossman, J.C., Wu, J., 2013. Defects activated photoluminescence in two-dimensional semiconductors: interplay between bound, charged, and free excitons. Sci. Rep. 3, 2657.

Wang, D., Li, X.-B., Han, D., Tian, W.Q., Sun, H.-B., 2017. Engineering two-dimensional electronics by semiconductor defects. Nano Today 16, 30–45.

Wätjen, J.T., Scragg, J.J., Ericson, T., Edoff, M., Platzer-Björkman, C., 2013. Secondary compound formation revealed by transmission electron microscopy at the Cu_2ZnSnS_4/Mo interface. Thin Solid Films 535, 31–34.

Wei, Z., Fung, C.M., Pockett, A., Dunlop, T.O., McGettrick, J.D., Heard, P.J., Guy, O.J., Carnie, M.J., Sullivan, J.H., Watson, T.M., 2018. Engineering of a Mo/SixNy diffusion barrier to reduce the formation of MoS_2 in Cu_2ZnSnS_4 thin film solar cells. ACS Appl. Energy Mater. 1 (6), 2749–2757.

Yan, C., Sun, K., Huang, J., Johnston, S., Liu, F., Veettil, B.P., Sun, K., Pu, A., Zhou, F., Stride, J.A., Green, M.A., Hao, X., 2017. Beyond 11% efficient sulfide Kesterite $Cu_2Zn_xCd_{1-x}SnS_4$ solar cell: effects of cadmium alloying. ACS Energy Lett. 2 (4), 930–936.

Yang, K.J., Sim, J.H., Jeon, B., Son, D.H., Kim, D.H., Sung, S.J., Hwang, D.K., Song, S., Khadka, D.B., Kim, J., Kang, J.K., 2015. Effects of Na and MoS2 on Cu2ZnSnS4 thin-film solar cell. Progr. Photovolt.: Res. Appl. 23 (7), 862–873.

Yazyev, O.V., Kis, A., 2015. MoS_2 and semiconductors in the flatland. Mater. Today 18 (1), 20–30.

Yim, C., O'Brien, M., McEvoy, N., Winters, S., Mirza, I., Lunney, J.G., Duesberg, G.S., 2014. Investigation of the optical properties of MoS2 thin films using spectroscopic ellipsometry. Appl. Phys. Lett. 104 (10), 103114.